Chinese Chemical Letters 35 (2024) 108460

Contents lists available at ScienceDirect

Chinese Chemical Letters

journal homepage: www.elsevier.com/locate/cclet

Imaging-guided precision oncotherapy mediated by nanoprobes: From seeing to curing

Jie Zheng[a], Shi-Hui Chen[a], Biao Huang[a], Mingxi Zhang[b], Quan Yuan[a,*], Ran Cui[a,c,*]

[a] College of Chemistry and Molecular Sciences, Wuhan University, Wuhan 430072, China
[b] State Key Laboratory of Advanced Technology for Materials Synthesis and Processing, Wuhan University of Technology, Wuhan 430070, China
[c] Hubei Jiangxia Laboratory, Wuhan 430200, China

ARTICLE INFO

Article history:
Received 26 November 2022
Revised 22 March 2023
Accepted 14 April 2023
Available online 15 April 2023

Keywords:
Precise theranostics
Imaging-guided
Tumor surgical navigation
Chemodynamic therapy
Phototherapy
Nanoprobes

ABSTRACT

Malignant tumors are the main diseases threatening human life. Using precise theranostics to diagnose and cure tumors has emerged as a new method to improve patient survival. Based on the current development of precise tumor imaging, image-guided tumor therapy has received widespread attention because it is beneficial for developing precise treatment of tumors, has the potential to improve the efficacy of tumor therapy and reduce the incidence of adverse side effects. Nanoprobes, which are nanomaterial functionalized with specific biomolecules, have intrigued intense interest due to their great potential in monitoring biorecognition and biodetection evens. Benefiting from the unique advantages of nanomaterials, including the easy surface functionalization, the unique imaging performances, and the high drug loading capacity, nanoprobes have become a powerful tool to simultaneously realize tumor precise imaging, diagnosis, and therapy. This review introduces the non-invasive tumor precise imaging and highlights the recent advances of image-guided oncotherapy mediated by nanoprobes in anti-tumor drug delivery, tumor precise surgical navigation, chemodynamic therapy, and phototherapy. Finally, a perspective on the challenge and future direction of nanoprobes in imaging-guided tumor theranostics is also discussed.

1. Introduction

Malignant tumors are one of the major diseases threatening human health and life [1,2]. In recent years, the incidence of tumors has gradually increased, and tumors have become the second leading cause of death in the world [3]. The identification, staging, and classification of tumors by precise non-invasive *in vivo* imaging technology is conducive to develop precise treatment for tumors, which is crucial for improving the curative effect of tumor treatment [4,5]. Traditional imaging techniques have been used in clinics, including computed tomography (CT), ultrasound (US), magnetic resonance imaging (MRI), and positron emission tomography (PET), *etc.* [5–7]. With the development of imaging technology and material science, the emergence of new imaging technologies, such as near-infrared fluorescence imaging and photoacoustic imaging, has further promoted the progress of non-invasive and precise tumor imaging [8,9]. Whether for traditional or new imaging techniques, ideal imaging probes are of great significance to improve imaging resolution, obtain important physiological information about tumors, and achieve accurate tumor diagnosis.

Nanoprobes, which are nanomaterial functionalized with specific biomolecules, have intrigued intense interest due to their great potential in monitoring biorecognition and biodetection evens [10,11]. Due to the unique properties of nanoprobes, they show unlimited potential in rapidly and accurately diagnosing tumors and further improving the curative effect of tumor therapy [12]. Nanoprobes have many unique properties: (1) The imaging performance can be optimized with the regulation of composition, size, or structure of nanoparticles, (2) the large specific surface area of nanomaterials is conducive to surface functional modification, which facilitates accurate molecular imaging of tumors, (3) appropriate composition adjustment of nanoparticles can endow them with the ability of multimodal imaging and even the treatment of tumors [13–15]. Therefore, the unique properties of nanoprobes make their application ideal for imaging probes, therapeutic agents, and drug carriers, and give them great advantages in precise tumor imaging, therapy, and imaging-guided tumor therapy [16,17].

The design and synthesis of nanoprobes will directly influence the final tumor imaging and therapeutic efficacy. Nanoprobes are usually composed of the following three parts: (1) core nanopar-

* Corresponding authors at: College of Chemistry and Molecular Sciences, Wuhan University, Wuhan 430072, China.
E-mail addresses: yuanquan@whu.edu.cn (Q. Yuan), cuiran@whu.edu.cn (R. Cui).

https://doi.org/10.1016/j.cclet.2023.108460
1001-8417/

ticles (NPs), (2) affinity layer, (3) targeting part. As the most important component of nanoprobes, core NPs can be selected from a variety of materials, such as metal NPs, quantum dots (QDs), carbon-based nanomaterials, magnetic NPs, silica NPs [18]. The large specific surface area and functional groups on the surface of NPs make them possible to connect with affinity layer and targeted components [19]. Moreover, antitumor drugs and dyes can be loaded on or inside the core particles. The combination of macromolecular affinity layer (*i.e.*, PEG, polypeptides, dextrans, chitosan, *etc.*) with core particles improves their hydrophilicity, improves their biocompatibility, and enhances NPs circulation time *in vivo* [20]. Targeting components (*e.g.* antibodies, peptides, aptamers) can be tailored to identify the receptors on tumor specifically to achieve target. In recent years, new targeting strategies which use cell-derived materials for functional modification have emerged [21], including cell-mediated (erythrocytes, macrophages, leukocytes, stem cells, tumor cells, *etc.*) NPs delivery, nonimmunogenic bacteria-mediated NPs delivery, extracellular vesicles-mediated NPs delivery, and biomimetic cell membrane coating-assisted NPs delivery. In general, a variety of nanoprobes with excellent performance have been constructed by optimizing the above three building blocks.

In this review, we focus on the application of nanoprobes in precise imaging and imaging-guided theranostics of tumors. Firstly, we introduce the recent process in the application of nanoprobes for precise tumor imaging. Secondly, we summarize the utilization of nanoprobes in imaging-guided tumor surgical navigation. Thirdly, related research about nanoprobes as carriers of antitumor drugs while providing real-time dynamic imaging to monitor the release of drugs is also introduced. Finally, we discuss the latest development of nanoprobes in imaging-guided tumor chemodynamic therapy and phototherapy. Based on these explorations, our thinking about current challenges and prospects for future research is proposed.

2. Nanoprobes for *in vivo* precise imaging of tumors

Precise imaging is critical for tumors diagnosis, staging and regulation of follow-up therapeutic regime. Developing high-contrast nanoprobes provides a promising opportunity for precise imaging of tumors. In this section, we focus on recent advances in nanoprobes that can be used for precise imaging of tumors *in vivo*.

2.1. For precise NIR-II fluorescence imaging of tumors

The near-infrared (NIR) window is more suitable for *in vivo* imaging as compared with visible light (400–700 nm) due to its reduced photon scattering and tissue autofluorescence [8,22]. The fluorescence imaging of tumors in the NIR window, especially fluorescent imaging in the second near-infrared window (NIR-II, 1000–1700 nm), has attracted considerable attention due to its ability to afford deeper penetration depth and higher clarity for *in vivo* images [23–25]. Thus, NIR-II fluorescent imaging can assist the diagnosis more accurately and provide more details for tumor treatments [26]. Over the past few years, a variety of fluorescent nanomaterials emitting in the NIR-II window with high fluorescence quantum yields have been designed for *in vivo* tumors imaging nanoprobes, including inorganic nanomaterials such as single-walled carbon nanotubes (SWNTs) [27], rare-earth nanoparticles (RENPs) [28–30], QDs [31–36] and organic nanomaterials such as semiconductor polymer nanoparticles (SPNs) [37]. Among these nanomaterials, those that can be used for multi-channel fluorescence imaging are ideal probes for precise tumor imaging. Since different types of immune cells in the tumor microenvironment (TME) may express the same surface antigens, the classification and staging of tumor cells require multi-channel imaging using dual- or even multi-target fluorescent probes to simultaneously confirm different characteristic molecules. Fluorescent nanoprobes with non-overlap emission in the NIR-II window or different fluorescence lifetimes, such as QDs or RENPs, can avoid mutual interference in multi-channel fluorescence imaging [38,39].

Nanoprobes based on QDs have offered tremendous promise in the precise imaging of tumors *in vivo*, due to the unique fluorescence properties of QDs, such as high light stability, emission-tunable, high fluorescence quantum yields, and tunable multicolor fluorescence [40,41]. Yu *et al.* constructed a PbS/CdS QD-based nanoprobes with non-overlap fluorescence emission in the NIR-II region for the two-color molecular imaging of *in vivo* myeloid-derived suppressor cells (MDSCs) [42]. PbS/CdS QDs emitting in NIR-IIa and NIR-IIb window respectively were conjugated with two different MDSC-specific antibodies to prepare the two-color targeting nanoprobe (Fig. 1a). Through the two-color molecular imaging and the high-resolution imaging of PbS/CdS QDs, the non-invasive accurate imaging of MDSCs was realized and the distribution of MDSCs was revealed for the first time. These results demonstrated that QDs-based nanoprobes with non-overlap emission in the NIR-II windows provided a useful tool for monitoring the change of immune cells *in vivo*, thus providing more physiological information about tumors and treatments. In addition, the silver chalcogenide (Ag_2X; X = S, Se, Te) QDs without toxic heavy metal elements are promising fluorescent materials for *in vivo* tumor imaging [43–46]. However, due to the narrow band gap, the emission wavelength of Ag_2X QDs is difficult to be precisely and continuously tuned in a wide wavelength range, and it is a challenge to obtain Ag_2X QDs imaging probes with non-overlap emission in the NIR-II window. Pang's group successfully solved the problem *via* trialkylphosphine-induced QDs ripening [47]. The precise regulation of the emission wavelength of Ag_2Te QDs was realized from 950 nm to 2100 nm (Fig. 1b). Ag_2Te QDs were synthesized by this strategy with emission wavelengths covering the entire NIR-II region. This work provides a novel strategy to control the growth processes of nanocrystals. In the future, NIR QDs with multicolor fluorescence emission spectra without toxic heavy metal elements will play a unique role in non-invasive tumor molecular imaging.

RENPs with long luminescence lifetime, low toxicity and narrow emission spectrum have become promising NIR-II bioimaging nanoprobes [30,48]. The NIR-II emission of RENPs comes from the down-conversion luminescence, and different luminescence lifetime imaging approaches based on RENPs contribute to achieving precise imaging of multi-target of tumors [28,49]. Zhang's group designed a NIR-II nanoprobe based on RENPs with core-multi-shell nanostructure and engineered luminescence lifetimes [29]. By changing the thickness of the energy relay layer or increasing the concentration of Er^{3+} in the inner layer, the nanoprobe realized a lifetime range spanning three orders of magnitude in a single emission. Three different lifetime populations of nanoparticles were conjugated with antibodies against three biomarkers for breast cancer to realize multi-target recognition of breast cancer cells (Figs. 1c and d). This strategy based on distinct lifetime channels of RENPs enables multi-target recognition of tumors and creates a fast and reliable real-time approach to identify tumor subtypes, whereby demonstrates its potential to detect multiple diseases simultaneously.

2.2. For enhanced photoacoustic imaging of tumors

Photoacoustic imaging (PAI) as an emerging non-invasive imaging modality with high sensitivity, high resolution, and deep tissue penetration, shows great potential in biomedical imaging [50–54]. In PAI, the tissues or PAI probes absorb optical energy and convert it to thermal energy under irradiation of a pulse laser, then they undergo a thermal expansion-relaxation process to generate an ul-

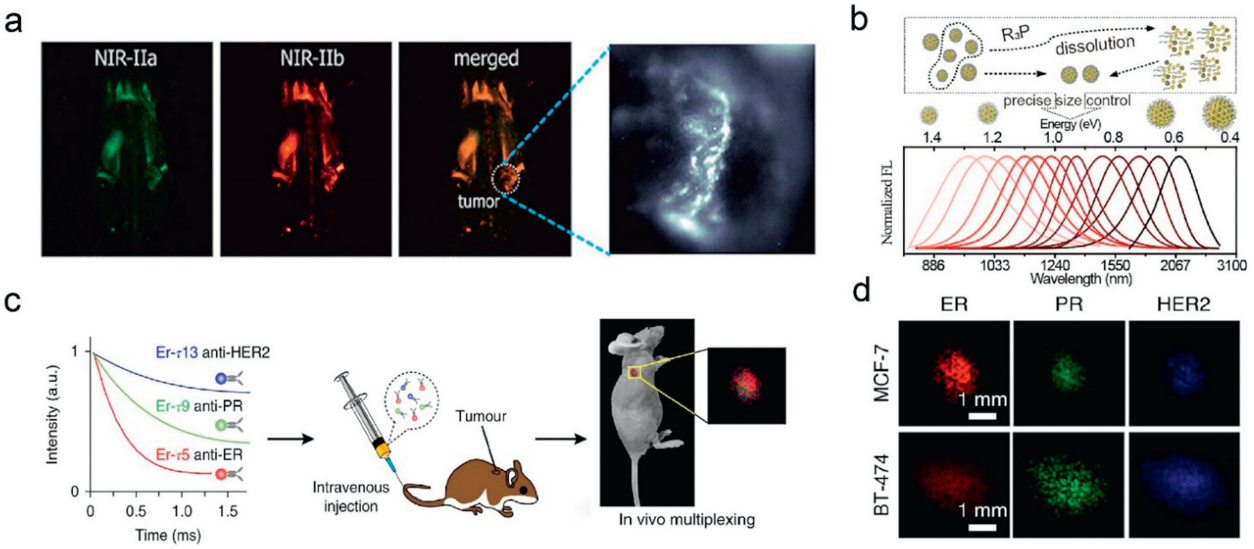

Fig. 1. *In vivo* precise imaging by NIR-II emitting inorganic nanoparticle-based probes. (a) *In vivo* non-invasive two-color fluorescence imaging of mouse possessing SCC7 xenograft and tumors in the NIR-II window. Copied with permission [42]. Copyright 2019, American Chemical Society. (b) Schematics of trialkylphosphine-controlled Ag_2Te growth and summaries of emission spectra of Ag_2Te QDs. Copied with permission [47]. Copyright 2021, American Chemical Society. (c) Illustration of *in vivo* tumor imaging using three lifetime populations of the Er nanoparticles. (d) Lifetime-resolved images of the MCF-7 and BT-474 tumors. Copied with permission [29]. Copyright 2018, Springer Nature.

trasonic signal, which is detected by an ultrasonic transducer and then the ultrasonic transducer reconstructs PA image by analyzing the ultrasonic signal [55–59]. Different from traditional X-rays CT and PET, PAI involves low-power nonionizing radiation, making it safer for living organisms [60]. The intensity of electromagnetic radiation and other factors will affect the generation of the final photoacoustic signal. Thermoelastic expansion models are widely studied in photoacoustic imaging. In thermoelastic expansion models, increasing laser fluence can lead to PA signal enhancement [61]. However, high electromagnetic radiation energy for enhancing laser fluence can also lead to degradation of PAI nanoprobes [62]. Therefore, optimizing the electromagnetic intensity is the key to generate optimal sound signals.

Endogenous targets with light absorption such as hemoglobin, lipid and melanin can produce strong photoacoustic signals, providing the possibility for tumor detection *in vivo* [63–65]. For example, melanoma-containing melanoma has been successfully detected by PAI [66]. However, in order to obtain high-contrast PA images of more diseased tissues, exogenous imaging probes are needed to improve the signal-to-background ratio of PA imaging. Thus, a variety of nanomaterials with excellent properties have been explored as exogenous imaging probes for PAI [67], such as metallic nanomaterials [68–70], transition-metal chalcogenides-based nanomaterials [71], semiconducting polymer nanoparticles (SPNs) [72] and QDs [73,74]. In recent years, the PAI nanomaterials that have strong NIR-II absorption were emerging and significantly improved the contrast and resolution of PAI due to the lower background signal of endogenous substances and reduced tissue scattering in the NIR-II window [75,76]. Gold nanoparticles (AuNPs) are important PAI contrast probes and have been generally employed because of the tunable absorption wavelength, strong optical absorption, and easy surface modification [77,78]. When the frequency of the incident photon matches the frequency of free charges on the surface of AuNPs, resulting in resonance and leading to strong optical absorption, the localized surface plasmon resonance (LSPR) effect occurs [79,80]. Due to the LSPR of Au NPs, when the size and shape of Au NPs are changed, the resonant frequency changes and further affects the optical absorption of AuNPs [81]. By manipulating their size and shape, AuNPs can generate strong absorption in NIR, resulting in stronger PA signals. The size, shape and surface state of gold nanoparticles will affect their interaction with environmental media and cells. Among them, the size of gold nanoparticles causes a general attention, because the size of gold nanoparticles ultimately determines their ability to cross physiological barriers and their toxicity to tissues [82,83]. Cheng *et al.* modified the surface of AuNPs with the PEG5000 (polyethylene glycol, Mn = 5000), which would promote cross-linkable under 405 nm laser and then generate a new absorption peak in NIR region (Figs. 2a and b) [84]. The strategy of light-triggered assembly of NPs to enhance PA signal can be further extended into other PA imaging probes so as to achieve advanced functions. Chen *et al.* adopted the strategy of adjusting the volume of gold nanorods (AuNRs) with similar aspect ratios to regular-sized AuNRs to realize the regulation of the absorption of AuNRs [85]. This study found that the relatively smaller AuNRs have shown stronger absorption at 1064 nm compared with the larger one among AuNRs with the same aspect ratio. And the smaller AuNRs generated 4.5 times greater PA signal at tumor site than the larger one. This finding also provides a new strategy for designing AuNPs-based nanoprobes with NIR-II absorption for PAI.

In addition to the characteristic of longer-wavelength absorption, the PAI probes also should have good thermal stability to obtain stable and high signal-to-noise ratio PA signals. Compared with AuNPs, transition-metal chalcogenide-based (TMC-based) nanoprobes have better thermal stability, because their structures hardly change under laser irradiation [86]. In addition, most TMC-based nanoprobes, such as WS_2, $Cu_{2-x}S$ (x = 0–1), TiS_2, and Bi_2S_3, inherently have high photothermal conversion efficiencies, which are conducive to acquiring enhanced non-invasive PA images *in vivo*. For example, $Cu_{2-x}S$ NPs serve as excellent PAI probes, whose composition and structure are easy to engineer. The absorption of $Cu_{2-x}S$ NPs in the NIR-II region can be achieved *via* adjusting the composition and structure of $Cu_{2-x}S$ NPs to improve the tumor imaging contrast [87]. As early as 2012, Ku *et al.* tuned the absorption peak of CuS NPs to longer wavelengths by adjusting the stoichiometric ratio of the synthetic precursors $CuCl_2$ and Na_2S, and $Cu_{2-x}S$ NPs as a promising PA imaging probe at 1064 nm

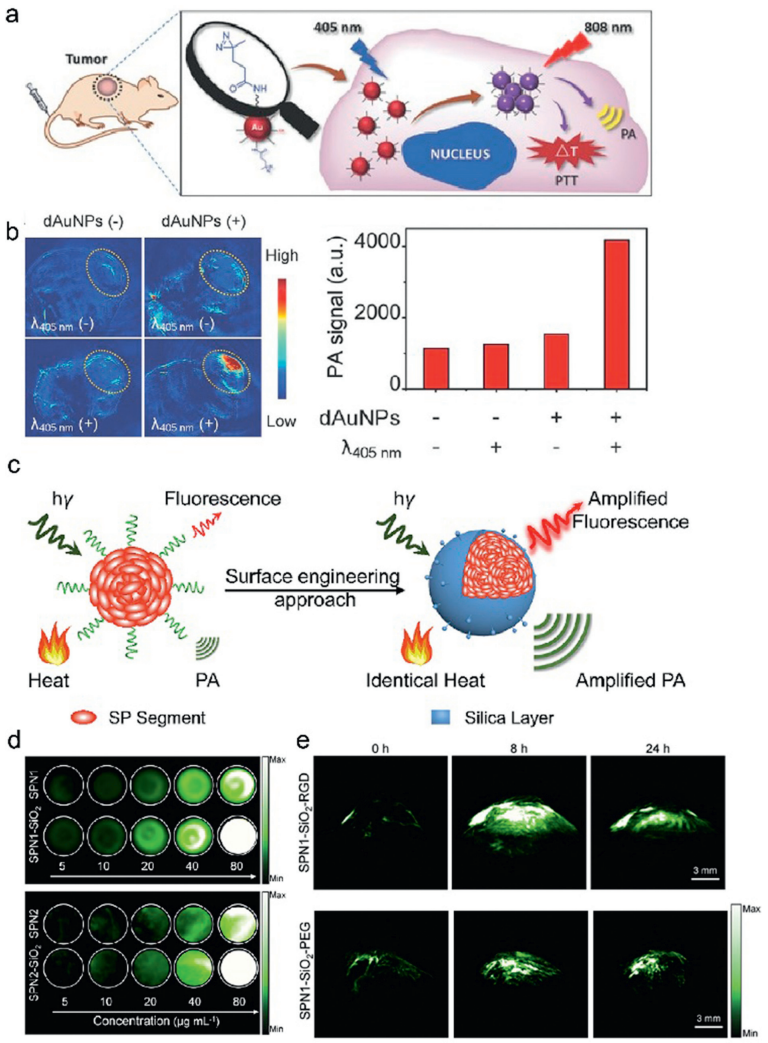

Fig. 2. Amplified PA imaging of dAuNPs and SPNs. (a) Schematic illustration of light-triggered assembly of AuNPs. (b) PA images and quantified PA signals of the tumorous sites of mice receiving treatments with different combinations. Copied with permission [84]. Copyright 2017, Wiley-VCH. (c) Scheme of surface engineering approaches for amplified PA imaging. (d) The PA images of two different SPN at different concentrations. SPN1, SPN1-SiO_2 (top) and SPN2, SPN2-SiO_2 (down). (e) PA images of subcutaneous tumor of SPN1-SiO_2-RGD and SPN1-SiO_2-PEG through tail vein injection for 0, 8 and 24 h, respectively. Copied with permission [90]. Copyright 2017, Elsevier.

can enhance tumor imaging [88]. This imaging approach has great potential for PAI in deep tissues.

Semiconductor polymer nanoparticles (SPNs) are an emerging class of ideal PAI nanoprobe for tumor imaging, consisting of organic and biological inert components (semiconducting polymers and amphiphilic polymers). SPNs generally possess high biocompatibility, excellent photothermal conversion efficiency, and photostability [89]. Pu's group has carried out a series of explorations in this field, and amplified the PA signal of SPNs at tumor sites *in vivo* through several different strategies [90–93]. For instance, they amplified the PA signals by coating SPNs with the silica layer (Fig. 2c) [90]. Since the interfacial thermal conductance between the silica layer and water is higher than that of semiconducting polymers, this effect consequently leads to a rapid temperature increase of SPN-SiO_2 under laser irradiation. The PA signals are enhanced in turn (Fig. 2d). After further surface modification, targeted imaging of tumor was demonstrated in mice, and the PA signal at the tumor site was also significantly amplified (Fig. 2e). In their other work, they revealed that the electron donor-acceptor backbone structure of SPs is the key factor determining PA signals of SPNs [94]. By increasing the electron-donating ability of the corresponding structural unit of DPP, SPNs show enhanced photothermal conversion efficiency. These strategies provide directions for the synthesis and modification of organic nanoparticles for molecular imaging. Besides that, SPNs encapsulated with amphiphilic copolymers not only possess overwhelming tumor imaging ability in the NIR-II region but also can be effectively degraded and cleared, thus exhibiting lower toxicity and higher biocompatibility *in vivo* [93]. The above strategies provide a new direction for gaining NIR-II PA imaging nanoprobes that are more suitable for *in vivo* tumor imaging.

2.3. For precise magnetic resonance imaging of ultrasmall tumors

Magnetic resonance imaging (MRI), with the advantages of noninvasive imaging and exquisite soft tissue contrast, has generally been employed in clinical tumor imaging [95]. MRI provides distinct images that reflect internal tissue information by detecting the relaxation time of water protons [96]. In order to clearly and accurately display the anatomical structure and location of the tumor and provide sufficient diagnostic information, we must pay attention to the imaging conditions and the selection of MRI probes [97]. Normally, the imaging conditions can be adjusted to obtain high-contrast images, such as magnetic field strength, frequency intervals. Higher magnetic field strength provides images with stronger signal-to-noise ratio [98]. On the other hand, the

frequency intervals between two radiofrequency pulses (repetition time) mainly affect T1-weight. Increasing repetition time will lead to the increase of longitudinal magnetization tendency of tissue [99]. The input of exogenous MR imaging probes can further increase the signal intensity of MRI by affecting the relaxation time of water protons [90,100]. The imaging probes for MRI are generally divided into T1-weighted and T2-weighted imaging probes. T1 imaging probes mainly include paramagnetic materials containing Gd, Fe, Mn, and other elements. And T2 MR imaging probes mainly focus on superparamagnetic iron oxide (SPION) [101,102]. Since the dark signal produced by the T2 imaging probe is not clear but the bright signal from the T1 imaging probe is easy to identify, T1 imaging probes are commonly used in clinical MRI. Gd-based complexes have been approved as T1 imaging probes for clinical tumor and tissue imaging, but commercial Gd-based imaging probes generally have low relaxation rates and potential nephrotoxicity, hindering their further application *in vivo* [103,104]. Therefore, the low toxicity T1 imaging probes with high relaxation rates are urgently needed.

Nanoprobes based on iron oxide nanoparticles and manganese(II) complexes with low toxicity have become powerful tools for targeting MR imaging of tumors, especially the small tumors [105–112]. Tiny tumors imaging *in vivo* which is critical for early tumor diagnosis is an extremely challenging area of research in MR imaging, due to the low non-specific absorption of imaging probes by small tumors. Conventional MR imaging probes are difficult to accumulate at tumor sites and contrast enhancement of MR imaging for ultrasmall tumors is limited. It is worth mentioning that due to the easy surface functionalization of nanoprobes, some of the iron oxide nanoparticles and manganese(II) complexes were facilitated for constructing the targeting probes of tiny tumors. For example, Ma *et al.* synthesized monodisperse Fe_2O_3 supraparticles (SPs), and Fe_2O_3 SPs were further disassembly into small-sized Fe_2O_3 NPs after efficient aggregation in the TME [112]. The Fe_2O_3 NPs express higher r1 values and lower r2/r1 ratio, due to their surface-to-volume ratio which facilitates the coordination interactions of water molecules and Fe_2O_3 NPs surface, and then affects the relaxation time of water protons. What is more, the small-sized Fe_2O_3 NPs also exhibited distinct renal clearance capacity and favorable biocompatibility. Based on the small-sized Fe_2O_3 NPs, tumors as small as 5 mm^3 could be identified precisely *in vivo* tumor imaging. Besides that, Li and colleagues conjugated manganese ferrite NPs (UMF NPs) with high r1 value and rapid renal clearance with cysteine-arginine-glutamic acid-lysine-alanine (Cys-Arg-Glu-Lys-Ala, CREKA), achieved accurate detection of ultrasmall metastases (Fig. 3a) [113]. UMFNP-CREKA possesses multilevel responsive signal-amplification capabilities and can release Mn^{2+} by binding with fibrin-fibronectin complexes around tumors under the stimulation of TME. The release of Mn^{2+} can amplify T1-weighted MR imaging signals and successfully detect metastases smaller than 0.39 mm, which is the smallest tumor that can be detected by MRI (Fig. 3b). These methods provide an effective strategy for the design of nanoprobes suitable for the precise imaging of ultrasmall tumors.

2.4. For multimodal imaging of tumors

Multimodal imaging generally combines imaging techniques with high penetration depth (PA, MRI, CT) and high temporal and spatial resolution (optical imaging, PET) [114,115]. In combination with the merits of different imaging modalities, it overcomes the limitations of a single imaging modality and can simultaneously reflect anatomical and biomolecular information of tissues *in vivo* [116]. Moreover, multimodal imaging can accurately depict the three-dimensional structure, location and edge of the tumor, and provides more precise guidance for tumor resection and treatment by performing high-resolution and three-dimensional (3D) imaging on the premise of ensuring a deep imaging depth. Designing nanoparticles to construct imaging nanoprobes with diverse properties for multimodal imaging not only avoids the repeated injection of imaging probes but also enables complementary imaging [117]. Therefore, multimodal imaging based on nanoprobes can not only become an ideal tool for non-invasive precise tumor imaging but also reflect the complex biochemical processes *in vivo*. Moritz F. Kircher *et al.* designed a triple-modality MRI-PAI-Raman (MPR) imaging nanoprobe and it was used for high-sensitivity and high-resolution imaging of the tumor margins, and delineating tumor 3D structure (Fig. 4a) [118]. MPRs consist of AuNPs as the core coated with a layer of Raman molecule tag *trans*-1,2-bis(4-pyridyl)-ethylene. To protect the Raman-active outer layer, the surface was covered with a silica coating. And 1,4,7,10-tetraazacyclododecane-1,4,7,10-tetraacetic acid (DOTA)-Gd^{3+} was modified on the silica coating, resulting in gold-silica-based surface-enhanced Raman scatting (SERS) nanoparticles with Gd^{3+}. The MPR nanoprobe could cross the blood-brain barrier and efficiently accumulate at orthotopic brain tumor sites, enabling orthotopic brain tumor imaging in living mice. It can not only perform three-channel co-identification of tumors by MRI, PAI, and Raman imaging, but also provide complementary tumor information. This three-modality imaging strategy achieved accurate localization of the whole brain tumor using MRI, then obtained a high spatial resolution 3D image of the tumor through PAI, and finally Raman imaging with highly sensitive surface imaging capabilities was been used to detect tumor margins (Figs. 4b and c). With the guidance of triple-modality imaging of MPR NPs, brain tumors in living mice could be precisely resected. This strategy can reflect the status of tumors from different levels, provide more precise information for tumor diagnosis, therapy, and prognosis, and point out a new direction for tumor precise therapy.

3. Nanoprobes for imaging-guided tumors surgical navigation

The advances in precise tumor imaging, which can more accurately locate tumors and identify tumor margins, make imaging-guided tumor resection possible. Since tumor margins should be determined and distinguished from normal tissue to make sure the surgeons can completely remove the tumor without damaging normal tissues, real-time high-resolution intraoperative imaging guidance is vital during tumor resection [119]. Traditional imaging techniques, such as ultrasound, MRI, CT, PET, are mainly used for the preoperative assessment of tumors. However, optical imaging, especially fluorescence imaging with high temporal and spatial resolution, can be applied alone or in combination with traditional imaging techniques to get high-resolution images of tumors to provide real-time guidance for tumor resection and improve the accuracy of surgery [120,121].

As mentioned above, *in vivo* fluorescence imaging based on the near-infrared window effectively avoids the interference of tissue auto-fluorescence, and can achieve sub-centimeter-level imaging depth and micron-level imaging accuracy, thus it is more suitable for intraoperative imaging *in vivo*. Although a variety of fluorescent molecules, such as indocyanine green (ICG), methylene blue, and 5-aminolevulinic acid (5-ALA), have been widely investigated as commercially available imaging probes for fluorescence image-guided cancer surgery [9,122]. Nanoprobes have many advantages in NIR-II fluorescence imaging of tumor due to their inherent physical and chemical properties. For example, the wavelength of nanoprobes can be adjusted by changing the size, composition and so on, which is significant for NIR fluorescence imaging, especially the NIR IIb imaging (emitting in longer-wavelength region) [123]. Owing to suppressed photon scattering and diminished autofluorescence, NIR-IIb fluorescence imaging can afford deeper tissue penetration with higher clarity [124]. Nowadays, the NIR-IIb

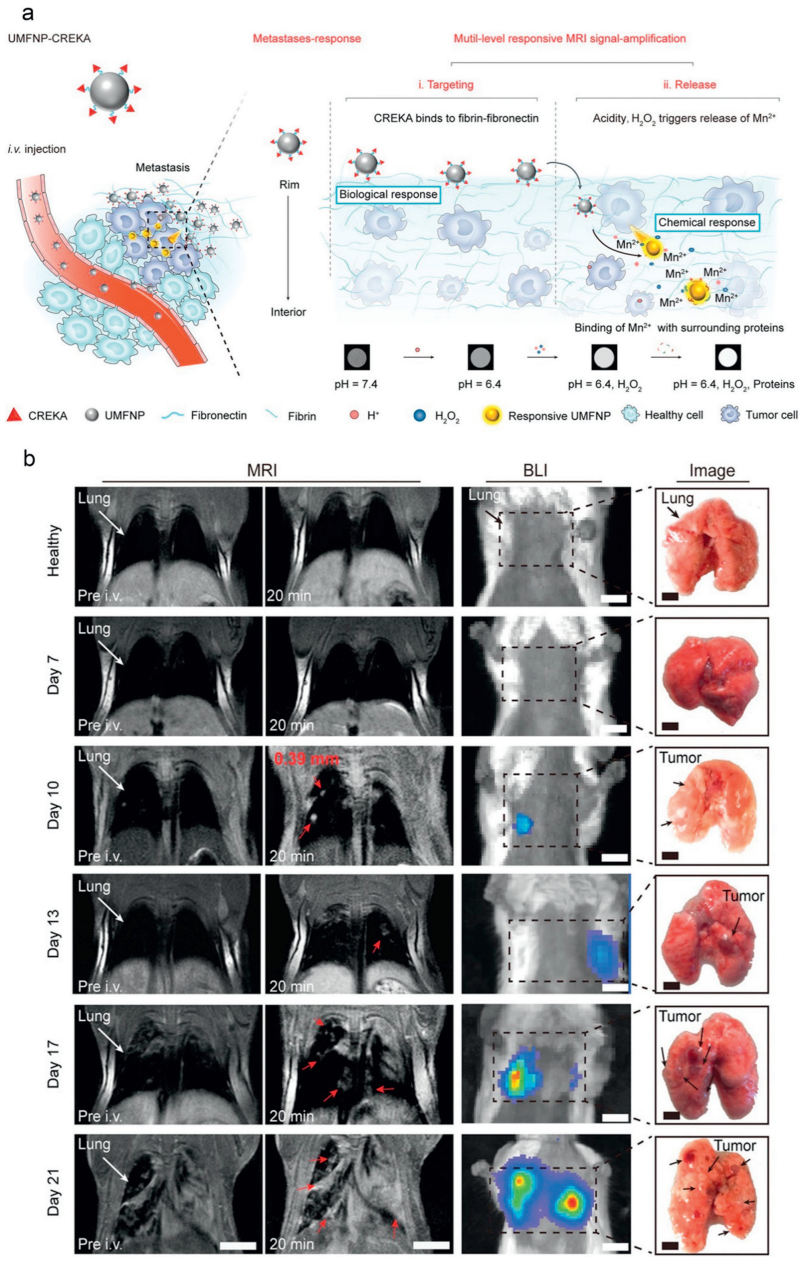

Fig. 3. *In vivo* T1-weighted MR imaging of ultra-small metastases by UMF NPs. (a) Schematic illustration of the bioinspired UMFNP-CREKA nanoprobe with multilevel responsive T1-weighted MR signal-amplification function for illuminating ultrasmall metastases. (b) MR images at 20 min post-injection with UMFNP-CREKA (left: pre-injection, right: post-injection, arrows indicate metastases; Scale bar = 5 mm) and BLI images (Scale bar = 5 mm) of mouse lung metastases. Copied with permission [113]. Copyright 2020, Wiley-VCH.

probes reported are mainly nanomaterials and the maximum emitting wavelength of most traditional fluorescent dyes reported is less than 1200 nm [125]. Besides, the large specific surface area of nanoprobes is conducive to surface functional modification, which is important for the further tumor targeting.

Emerging imaging nanoprobes have displayed wide potential application in imaging-guided tumor surgery because of their special function, structure, and outstanding properties [126]. For example, in the treatment of breast cancer, targeted excision and biopsy of tiny sentinel lymph nodes (LN) are the dominant ways to monitor tumor-lymph node metastasis, which are the key to formulating therapeutic regimes and tumor staging. The complete excision of tiny sentinel LNs requires the guidance of high spatial resolution imaging. Accordingly, Chen's group reported a multiplexed NIR-II fluorescent imaging method for visualization of primary/metastatic breast cancer and sentinel LNs using donor-acceptor-donor dye (IR-FD) with emission wavelengths in NIR-IIa (1100–1300 nm) and PbS/CdS QDs with emission in the NIR-IIb (1500–1700 nm) window during the surgery, respectively (Fig. 5a) [127]. In this study, IR-FD was used to map primary/metastatic breast cancer cells. Since PbS/CdS QDs have high fluorescence quantum yields in the NIR-IIb region, they can provide better spatial resolution, thereby realizing precise resection of tiny sentinel LNs guided by NIR-IIb fluorescence imaging (Figs. 5b and c). With the dual-NIR-II guidance of the two NIR-II fluorescent probes, real-time surgical navigation could be achieved. Moreover, the multiplexed NIR-II imaging system has the ability to predict tumor metastasis in the process of intraoperative excision of sentinel LNs, further reducing the time for biopsy judgment, and saving time for tumor treatment.

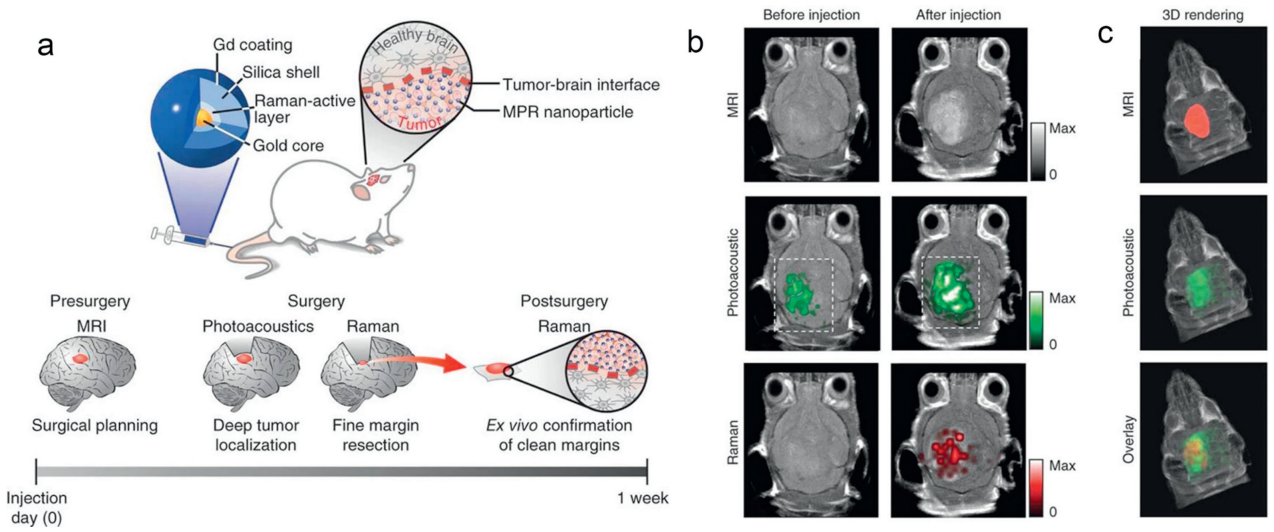

Fig. 4. *In situ* non-invasive triple-modality MRI-PAI-Raman imaging of brain tumor by MPR NPs. (a) Triple-modality MPR concept. (b) Two-dimensional axial MRI, photoacoustic and Raman images. The post-injection images of all three modalities showed clear tumor visualization. (c) A three-dimensional (3D) rendering of magnetic resonance images with the tumor segmented (red; top), an overlay of the three-dimensional photoacoustic images (green) over the MRI (middle) and an overlay of MRI. Copied with permission [118]. Copyright 2012, Nature Publishing Group.

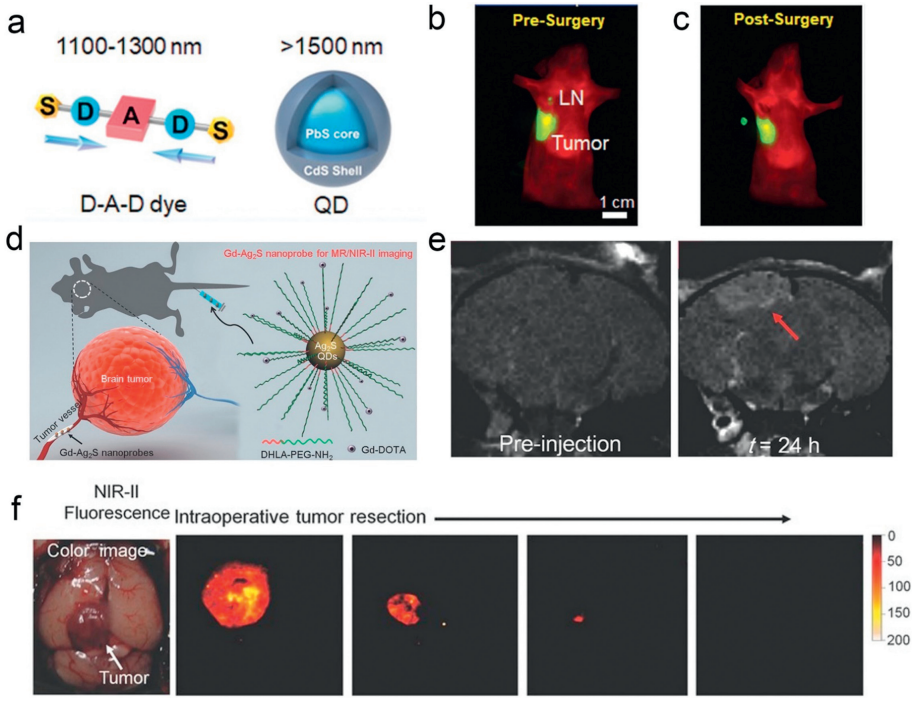

Fig. 5. NIR fluorescence imaging-guided surgical resection of tumors and sentinel lymph nodes. (a) Dual NIR-II probes design with donor-acceptor-donor (D-A-D) dye at NIR-IIa and PbS QDs at NIR-IIb. (b) Dual-NIR-II imaging of tumor and sentinel LN. (c) The dual-NIR-II imaging guided sentinel lymph node surgery in orthotopic 4T1 breast cancer model. Copied with permission [127]. Copyright 2020, Wiley-VCH. (d) Schematic illustration of the procedure for preparing Gd-Ag_2S nanoprobe and brain tumor targeting of Gd-Ag_2S nanoprobe. (e) T1-weighted MR images of U87MG brain tumors at different time points after injection of Gd-Ag_2S nanoprobe. (f) NIR-II fluorescence guided brain tumor resection using Gd-Ag_2S nanoprobe. Copied with permission [128]. Copyright 2015, Wiley-VCH.

Multimodal imaging that combines NIR fluorescence imaging with clinical imaging techniques is another way to accurately identify and resect the deep orthotopic tumors and brain tumors [124,128]. The multimodal imaging techniques through high spatial resolution intraoperative NIR fluorescence can delineate the precise macroscopic structure and localization of the tumor during the surgery. For example, Yan and colleagues designed a stimuli-responsive *in situ* self-assembly probe to activate multimodality imaging signals at tumor sites for imaging-guided tumor resection [129]. The probe they constructed consists of three parts: (1) a NIR fluorophore (merocyanine, Cy-Cl) capped by alkaline phosphatase (ALP) recognition phosphate group (-PO_3H), (2) a DOTA-Gd chelate for MR imaging and (3) a hydrophobic dipeptide Phe-Phe (FF) linker that promotes self-assembly. Under the activation of endogenous ALP, P-CyFF-Gd probe can dephosphorylation and self-assembly to form nanoparticles, and its fluorescent and MRI signals are greatly enhanced. The MR images can assist in spatially localizing ALP-positive tumors in the whole body *in vivo*, and NIR fluorescent signals can detect the edges of tumors. With the guidance of dual-modality imaging, the orthotopic liver tumor can be iden-

tified and resected. In another work, Wang's group reported a Gd-Ag_2S nanoprobe combining two imaging modalities (NIR-II fluorescence imaging and MRI) to guide the resection of the brain tumor precisely (Fig. 5d) [128]. Since brain tumors are closely associated with considerable brain structures and nerve cells, exact identification of the margin of brain tumor is critical for removing brain tumors and reducing irreversible damage. After accurately locating the depth of the brain tumor by MRI (Fig. 5e), NIR-II fluorescence imaging clearly distinguishes the edge of the brain tumor, and the brain tumor is precisely resected under its guidance (Fig. 5f). The above multimode imaging-guided tumor resection is a promising strategy in future clinical applications.

In order to achieve complete tumor resection, the optimal nanoprobes for image-guided tumors surgical resection should have the following characteristics: (1) Specific targeting to tumors. (2) High brightness and deep tissue penetration to ensure accurate tumor identification. (3) Adequate retention time to ensure high contrast imaging of tumor during surgery and to avoid repeated administration during surgery [130].

4. Nanoprobes for monitoring anti-tumor drug delivery

Real-time monitoring of drug biodistribution and pharmacokinetic studies are critical for precision tumor therapy. Based on the current development of precise tumor imaging, it is an important research field to realize the visualization of drug delivery by developing a drug delivery system with the imaging function to realize the evaluation of tumor treatment effect [131,132]. Currently, the visualized drug delivery systems generally consist of the following three parts: (1) therapeutic drugs, (2) imaging probes, and (3) drug carriers [133–136]. An ideal drug delivery platform should have the ability to maintain the drug within a desired therapeutic range. On the other hand, it should be able to control drug release at the tumor site under internal or external stimuli, to reduce its toxicity on surrounding normal tissues. Compared with conventional drug delivery platforms, due to the unique properties of nanomaterials, nanoprobes-based drug delivery systems with anti-tumor drug and imaging nanomaterials are widely employed in various aspects, such as real-time monitoring of the targeted drug delivery and extending the circulation time *in vivo* [137,138].

Nanoprobes as drug carriers play an important role in tumor targeting. Nanomaterials have a large specific surface area and rich surface functional groups, which possess natural advantages in surface modification and functionalization. When the surface of the carrier is functionalized with ligands (antibodies, peptides, RNA, *etc.*), the carrier can be specifically bound to the target to achieve specific recognition of tumor and TME [139]. In recent years, given the increased understanding of the key role of TME in regulating cancer progression and therapeutic effect, TME is regarded as a potential target for drug delivery [140]. The normal cells in TME were more genetically stable than tumor cells, and the genomic stability is helpful to reduce the influence of tumor heterogeneity [141]. Therefore, nanoprobes that target tumor microenvironment might be more universality.

The following approaches are widely used to construct a nanoprobe-based drug delivery system that can be released at the TME: (1) utilizing nanoparticles that can be decomposed in TME as carriers, such as amphiphilic polymer self-assembled nanoparticles [142], (2) encapsulating drugs and nanocarriers with compounds that decompose and release drugs under certain stimuli [143], (3) attaching antitumor drug molecules onto the surfaces of nanocarrier *via* chemical bonds that sensitive to changes in TME (the acidic pH, reductive environment, *etc.*) or external photothermal conditions [144]. For example, Lu *et al.* synthesized a dual responsive nanocarrier that released doxorubicin (DOX) in response to dual stimuli in the TME [145]. Specifically, the core-shell Fe/Gd hybrid NPs (FeGdNPs) were modified with methoxy poly(ethylene glycol) (mPEG) to load DOX, and then formed SA-FeGdNP-DOX@mPEG by self-assembly after aggregation. After SA-FeGdNP-DOX@mPEG efficiently aggregated at the tumor site, the acid-labile benzoic imide was cleaved under acidic conditions and the glutathione-labile (GSH) linker disulfide bond on cystamine dihydrochloride (CA) could be broken under reductive conditions, leading to dissociation of its self-assembled structure and release of DOX. In particular, due to the tight assembly of SA-FeGdNP-DOX@mPEG, an acidic or reductive environment cannot make it dissociated. Therefore, DOX exhibits pH/GSH dual stimulus-responsive release ability, which can effectively reduce adverse side effects of DOX release in normal tissues. Importantly, since the r2 value is proportional to particle size and the saturation magnetization, the r2 value of the decomposed nanoparticles in the TME is much tinier than that before the decomposition, resulting in a decrease in the r2/r1 ratio. Consequently, the T1-weighted MRI positive signal was presented in tumor site, while SA-FeGdNP-DOX@mPEG cannot disassemble in normal tissue, which showed a high r2/r1 and T2-weighted negative signal. This smart MRI signal switch in the TME can significantly enhance the contrast of MRI at the tumor site, track the distribution of drugs and evaluate the therapeutic effect of tumor. This strategy realizes multiple response modes triggered by two or more stimuli, providing a new idea for building the ideal imaging-guided tumor chemotherapy platform.

Using nanoprobes with inherent imaging capabilities as drug carriers is an emerging strategy for the anti-tumor drug delivery, which benefits are improving atom utilization and reducing the amount of external agents injection and the unpredictable mutual interference between components [146,147]. For example, mesoporous silica NPs have been used as carriers for anti-tumor drugs due to their high loading capacity [143,147]. Since mesoporous silica NPs cannot be used as imaging probe, in order to realize the visualization of drug delivery, it is usually labeled with fluorophores. However, Chen *et al.* obtained the fluorescent mesoporous silica nanoparticles (FL-SiO_2 NPs) by calcining mesoporous silica particles containing amine (from 3-aminopropyltriethoxysilane (APTES)), and the fluorescence of FL-SiO_2 comes from carbon dots produced by calcining APTES [148]. When DOX is loaded into it, the real-time monitoring of the distribution of the mesoporous silica and loaded drug can be accomplished without using external fluorophore labeling. Such strategies of monitoring drug delivery by multifunctional nanoprobes can greatly promote atom utilization, thus improving the biocompatibility.

5. Imaging-guided tumors chemodynamic therapy and phototherapy based on nanoprobes

5.1. Imaging-guided tumor chemodynamic therapy

Chemodynamic therapy (CDT), a novel cancer therapeutic method, utilizes the Fenton reaction mediated by iron or the Fenton-like reaction initiated by other metal ions (such as Co^{2+}, Ti^{3+}, Ni^{2+}, Cu^{2+}, Mn^{2+}) to convert intracellular H_2O_2 to hydroxyl radical ($^{\bullet}OH$) [149–151]. The $^{\bullet}OH$ can cause irreversible oxidative damage to biomolecules such as lipids, proteins and deoxyribonucleic acid (DNA), thereby causing damage to target cancer cells [152–154]. Compared with normal cells, the content of H_2O_2 in the TME is higher, and the unique acidic conditions in it also facilitate the efficacy of the Fenton reaction and the Fenton-like reaction, so CDT has better selectivity in specifically eliminating tumor cells [155]. Meanwhile, the metal-based nanomaterials that are used to catalyze the Fenton reaction, such as iron-based and copper-based nanomaterials, also serve as versatile nanoprobes for tumor imaging. For this reason, imaging-guided CDT can be realized using Fen-

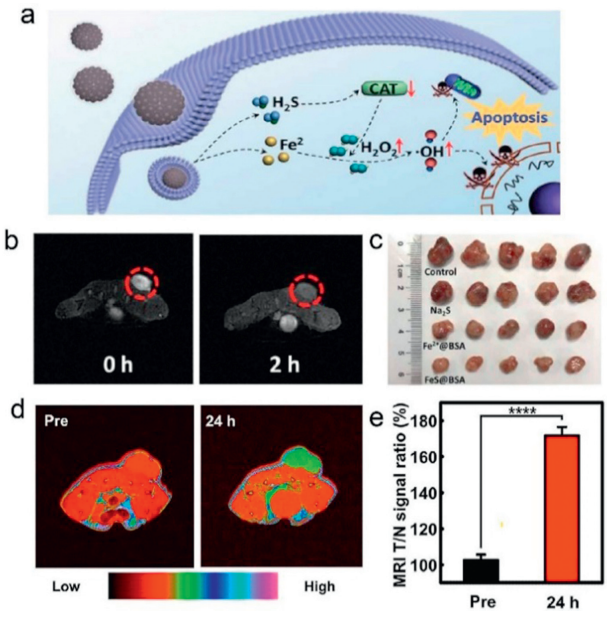

Fig. 6. MR imaging-guided chemodynamic therapy by FeS@BSA nanoclusters and Cu-Fe peroxide nanoparticles. (a) Schematic illustration of synergistic therapeutic mechanism of FeS@BSA nanoclusters. (b) T2-weighted MR images of Huh7 tumor-bearing nude mice before and after the intravenous administration of FeS@BSA nanoclusters for 2 h. (c) Photograph of the tumors extracted from the mice groups treated with different samples. Copied with permission [164]. Copyright 2020, Wiley-VCH. (d) *In vivo* T1-weighted MR images of a U-87MG tumor-bearing mouse before and 24 h after injection of Cu-Fe peroxide nanoparticles. (e) MRI signal intensity ratios of tumor-to-normal tissues. Copied with permission [168]. Copyright 2022, American Chemical Society.

ton metal-based nanoprobes to real-time monitor their distribution *in vivo* and therapeutic effect [156,157]. The examples of recently developed nanoprobes for imaging-guided chemodynamic therapy were shown in Table S1 (Supporting information).

As we all know, iron-based nanoprobes can not only show catalytic activity to produce ·OH, but also serve as MR imaging probes for bioimaging [158,159]. Since iron-based nanoprobes were employed as Fenton reagents for MRI-guided CDT in 2016, researchers have been striving to improve the effect of MRI-guided CDT [160]. On the one hand, the effect of tumor CDT is closely related to the TME. Decreasing the pH value and increasing the H_2O_2 level to enhance the efficiency of ·OH generation are two main approaches to improve the CDT of the tumor [161–163]. In a study by Xie and colleagues, the amorphous FeS@BSA nanoclusters were formed through embedding Fe^{2+} and S^{2-} in bovine serum albumin (BSA) using the self-assembly method [164]. In the acidic environment of the tumor, the FeS@BSA nanoclusters degrade and generate Fe^{2+} and H_2S (Fig. 6a). As an effective T2-weighted MRI imaging probe, Fe^{2+} presents a dark signal at the tumor site, so the release of Fe^{2+} at the tumor site can be observed by MRI signal changes to further guide the subsequent therapeutic effect (Fig. 6b). The generated H_2S regulates the functions of catalase (CAT) in cells, increasing the content of H_2O_2 in the TME, thereby also improving the efficacy of reactive oxygen species (ROS)-based therapeutic approaches [165]. The synergistic effect of FeS@BSA nanoclusters has significantly enhanced the anti-tumor effect (Fig. 6c). This method provides a new method for designing a synergistic diagnosis and treatment integrated nanoprobe of tumors with imaging guidance function.

On the other hand, since the efficiency of Fe^{3+} catalyzing Fenton reaction is lower than that of Fe^{2+} and the conversion from Fe^{3+} to Fe^{2+} is usually slow, it is important to improve the conversion efficiency between Fe^{3+} and Fe^{2+} to increase the efficiency of CDT [166,167]. Sagang Koo *et al.* designed a kind of Cu-Fe peroxide nanoparticles (CFp NPs) with polyvinylpyrrolidone (PVP) as a stabilizer [168]. Protonation of PVP in the acidic environment of tumors enables CFp NPs to release iron and copper ions. Cu^+ can not only regulate the charge transfer between Fe^{3+} and Fe^{2+} ($Cu^+ + Fe^{3+} \rightarrow Cu^{2+} + Fe^{2+}$), but also improve the efficiency of catalyzing the Fenton-like reaction to generate ·OH. Besides, the Cu^{2+} generated in this process also catalyzes the Fenton-like reaction to generate ·OH. The entire reaction process of the nanoparticles greatly improves the ·OH generation efficiency at the tumor site, and the released iron ions enhance the T1-weighted MRI signal (Figs. 6d and e). This imaging-therapeutic integrated nanoprobe that dynamically changes with the treatment process provides a new direction for personalized therapies.

Compared with iron-based nanoprobes, copper-based nanoprobes have a wider reaction pH range and higher ·OH yield, and the photothermal conversion ability enables them to realize the synergy of CDT and photothermal therapy under the guidance of PA imaging [169–171]. For example, Hu *et al.* reported for the first time that copper-based nanocatalysts have the ability to catalyze H_2O_2 into ·OH in a wider pH range [170]. The prepared ultrasmall $Cu_{2-x}S$ nanoparticles ($Cu_{2-x}S$ NPs) as the novel Fenton nanocatalysts for tumor therapy can not only kill cancer cells by efficiently decomposing H_2O_2 overexpressed in the TME into ·OH but also the $Cu_{2-x}S$ NPs can act as photothermal agents which can increase the temperature at the tumor site. Taking the unique advantage of copper-based nanomaterials, they can efficiently delineate/monitor the tumor regions with the help of PA images and enhance tumor therapeutic efficacy by CDT and photothermal therapy, thus enabling imaging-guided synergetic therapies.

5.2. Imaging-guided tumor phototherapy

Photodynamic therapy (PDT) and photothermal therapy (PTT), two typical phototherapy strategies, have attracted attention due to their negligible drug resistance, noninvasive properties, and low adverse side effects [172]. Photosensitizer is excited under laser irradiation, and then the excited state photosensitizer can generate ROS, in turn resulting in oxidative damage to cells and achieving a therapeutic effect [173–175]. PTT is a treatment method in which photothermal agents convert light energy into heat under laser irradiation, thereby increasing local temperature thermally ablating tumor cells [176,177]. The light range of phototherapy can be artificially controlled in space to irradiate specific sites, endowing it with selectivity and reducing side effects of photodamage to normal tissue [172]. Therefore, by evaluating the accumulation of phototherapy agents at the tumor site by imaging, including photothermal (PT) agents and photosensitizers (PSs), the laser dose can be tuned while ensuring the therapeutic effect so as to achieve the effect of precise therapy [178]. Furthermore, the phototherapy agents with imaging function can also be used to monitor the drug release process and predict the treatment effect during phototherapy. There are two main strategies for constructing nanoprobes that can be used for optical imaging-guided phototherapy: (1) single nanoplatforms with both the therapeutic and imaging functions; (2) combining multiple functional units such as the imaging probe and the phototherapeutic agent into one system of nanoplatforms [179,180]. Besides, due to the use of lasers during phototherapy, optical imaging (fluorescence imaging and photoacoustic imaging) is a common strategy in the study of imaging-guided tumor phototherapy [181,182]. The performance of nanoprobes used for optical imaging-guided phototherapy are summarized in Table S2 (Supporting information). In addition, the components of nanoprobe that play a key role in imaging and treatment are given in the table.

5.2.1. For NIR fluorescent imaging-guided tumor phototherapy

As mentioned above, due to the deep penetration depth of NIR light and less tissue scattering, fluorescence imaging-guided tumor phototherapy in NIR region is an important emerging research field in recent years [183–185]. A great variety of inorganic nanoprobes, such as rare-earth-doped nanocrystals [186], carbon-based nanomaterials [187–189], and a variety of organic nanoprobes can be used in NIR-I (700–800 nm) for fluorescence imaging-guided phototherapy. The guidance of high-resolution fluorescence imaging-guided phototherapy helps to improve the effect of tumor treatment. The content of O_2 during PDT is significant to the production of ROS, but the hypoxic TME greatly weakens the effect of O_2-dependent PDT. Therefore, it is urgently needed to construct a nanoplatform that can deliver or generate O_2 to improve the effect of PDT, and to monitor relevant parameters and evaluate the effect of PDT treatment in real time during the treatment process [190–192]. Jia *et al.* successfully prepared magnetofluorescent carbon dots (Mn-CDs) for the first time [193]. The presence of Mn^{2+} in Mn-CDs could react with H_2O_2 to generate MnO_2, and MnO_2 highly catalyzed H_2O_2 to generate oxygen, which ameliorated the hypoxic state of the TME and improved PDT efficiency. More importantly, the paramagnetic manganese (II) produced by acidic H_2O_2 reduction was an effective T1-weighted MR imaging probe. Therefore, Mn-CDs achieved fluorescence and MR dual-modality imaging-guided PDT. The tumor growth could be completely inhibited with no recurrence after the precise imaging-guided PDT.

The aggregation-induced emission luminogens (AIEgens) show much enhanced emission and some of them possess strong photosensitizing ability in aggregate state, which make them become promising turn-on probes for image-guided photodynamic therapy [194]. For example, Mao and colleagues designed a NIR-driven immunostimulant by covalently linking AIE photosensitizer TPEBTPy with SiO_2 up-conversion nanoparticles (UCNPs) [195]. AIEgen-coupled UCNPs show intense fluorescence after aggregating at the tumor site, and they can generate high-dose ROS, which excites PDT and induces immunogenic cell death under high-power NIR irradiation. AIEgen-coupled UCNPs can also capture the antigen released by tumor through electrostatic interaction and taken up by sentinel lymph nodes. Upon subsequent low-power laser irradiation of lymph nodes, low-dose ROS are produced to trigger effective T-cell immune response. This dual-mode ROS activation provided a powerful and controllable platform to active efficient antitumor immunotherapy.

For organic NPs-based nanoprobe, current research on the fluorescence imaging-guided phototherapy mainly focuses on overcoming the instability and non-specificity of phototherapy agents and small molecule dyes [196]. Conjugation or encapsulation of phototherapy agents and small molecule dyes to form organic nanoparticles with suitable carriers are widely used strategies [197]. For instance, Ren *et al.* successfully synthesized organic compounds ($C_{72}H_{82}N_2O_4S_3$)n (C3) with excellent photothermal properties, encapsulated with indocyanine green (ICG) into polyethylene glycol and polycaprolactone (PEG-PCL) to form hybrid nanoparticles (PEG-PCL-C3-ICG NPs) [198]. The NPs generate heat and ROS *via* C3, and realized fluorescence imaging through ICG, making NPs can be used for fluorescence imaging-guided PDT and PTT of tumors. PEG-PCL increases the photostability of ICG and avoids rapid ICG clearance at the tumor site, thereby enhancing PDT therapeutic efficacy. With the guidance of fluorescence images, the best laser irradiation timing can be confirmed to achieve a better tumor elimination effect. With this hybrid strategy, the instability and non-specificity of small molecule dyes could be greatly improved.

Compared with the NIR-I window, the NIR-II window has less interference from scattering and biological autofluorescence and can realize higher-resolution fluorescence imaging. Utilizing NIR-II fluorescence imaging technology enables real-time monitoring of tumor vascular morphological changes during phototherapy, enabling us to gain a deeper understanding of the interaction between phototherapeutic agents and tumor blood vessels, evaluate the therapeutic effects and guide subsequent treatment [199]. Since tumor blood vessels are the lifeline of tumor growth, developing special phototherapy agents with NIR-II imaging function is essential to achieve high-resolution imaging of tumor blood vessels and adjust the therapeutic regime by judging the reduction of tumor blood vessels during phototherapy by imaging [200,201]. For example, Huang *et al.* developed an arginine-glycine-aspartate (RGD) peptide-modified NIR-IIb PbS/CdS-RGD nanoprobe which has a long emission wavelength (-1600 nm) and good photothermal conversion performance (47.6%) [200]. Based on the high signal-to-background ratio advantage of the NIR-IIb imaging window, high-resolution fluorescent images can be obtained to reflect the vascular structure inside the tumor. The times of photothermal therapy were adjusted according to the monitoring of tumor blood vessel destruction by NIR-IIb fluorescence imaging. The NIR-IIb fluorescence images also could confirm that the intratumoral vascular network was completely ablated after PTT and excellent therapeutic efficacy was achieved with suppressed recurrence. This strategy offers a more precise imaging tool to judge the effect of phototherapy treatment on personalized therapies.

5.2.2. For photoacoustic imaging-guided tumor phototherapy

Photoacoustic imaging probes, which have good photothermal conversion efficiency, are a class of phototherapeutic agents with excellent performance [202–204]. In order to improve the resolution of photoacoustic imaging to better guide the phototherapy, many efforts have been made to develop nanoprobes with excellent performance in the NIR region. The nanoprobes widely employed in photoacoustic imaging-guided PTT and PDT mainly include gold nanoparticles [205], transition metal chorionic compounds [206], quantum dots [207], organic polymer nanoparticles and so on [208].

Nanoprobes with two-dimensional (2D) nanoplate structure have strong absorption and high photothermal conversion efficiency in the NIR region [209]. For example, transition metal dichalcogenide (TMDs) nanosheets are widely employed as photoacoustic imaging probes and photothermal agents because of their high photothermal conversion efficiency [210,211]. Zhu *et al.* prepared polyvinylpyrrolidone (PVP)-modified CoFeMn dichalcogenide nanosheets (CFMS-PVP NSs) using a lamellar CoFeMn-layered double hydroxide as a precursor for the first time [153]. The photothermal conversion efficiency can reach 89% by tuning the Co/Fe/Mn ratio in the layered double hydroxide (LDH) precursor, which is the highest photothermal conversion efficiency reported in 2D TMDs. Fe^{2+}, Fe^{3+} and Co^{2+} in CFMS-PVP NSs can convert H_2O_2 to $^{\bullet}OH$ through Fenton and Fenton-like reactions at the tumor site to kill tumor cells, while Mn^{4+} and Mn^{3+} can rapidly consume GSH through redox reaction, synergistically improving the CDT efficiency. The accumulation of CFMS-PVP NSs at the tumor site could be monitored according to the PA signal (Fig. 7a). With the guidance of PA images, the timing of photothermal therapy to the tumor could be confirmed, and tumors were completely eradicated in tumor-bearing mice by the combined PTT/CDT effects of the CFMS-PVP NSs (Fig. 7b). The CFMS-PVP NSs are one of the potential ideal tools for clinical imaging-guided tumor therapy in the future.

Besides, QDs-based nanoprobes have attracted much attention in PA imaging-guided phototherapy, especially all-in-one QDs [212]. Imaging-guided PDT/PTT combined therapy using all-in-one quantum dots does not require additional photosensitizers, avoids interference between components in the composite system, improves therapeutic effect with few side effects. Ding and col-

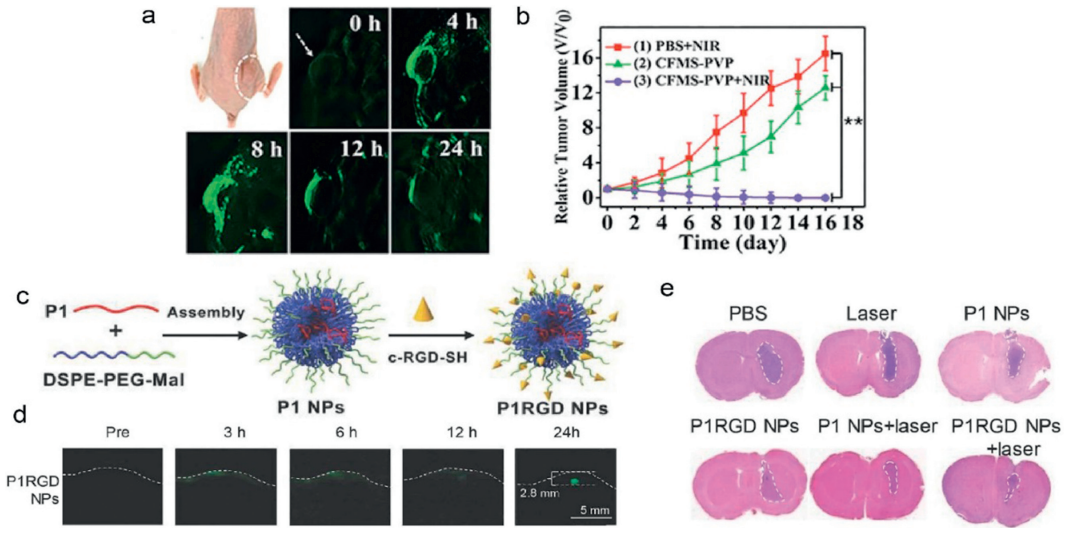

Fig. 7. Photoacoustic imaging-guided phototherapy of tumors *in vivo* by CFMS-PVP NSs and donor-acceptor structured P1-RGD NPs. (a) PA images of tumors tissue (arrows) at different time points after injection of CFMS-PVP NSs. (b) Relative tumor volume changes among treatment groups before and after CFMS-PVP NSs treatment. Copied with permission [153]. Copyright 2020, Wiley-VCH. (c) Schematic illustration of P1 NPs fabrication. (d) Through scalp and skull noninvasive PA imaging of mouse brain tumor at different time points upon P1-RGD NPs injection. (e) *In vivo* PTT of mice bearing orthotopic brain tumors. Copied with permission [217]. Copyright 2018, Wiley-VCH.

leagues used MoO_{3-x} QDs to construct multifunctional therapeutic nanoprobes for PA imaging-directed PDT/PTT combination tumor therapy [73]. The strong optical absorption of MoO_{3-x} QDs in NIR region enables the simultaneous generation of ROS and hyperthermic effects at the same time as executing PA imaging-guided PDT/PTT. Both *in vivo* and *in vitro* tests demonstrated that the generation of ROS and heat by 880 nm laser irradiation was sufficient to kill tumor cells when the PA signal was the strongest. Note that after being treated with the PDT/PTT combined tumor treatment, tumors in mice were completely ablated. This study paves the way to design the all-in-one nanomaterial probe for imaging-guided PDT/PTT combined tumor treatment.

Donor-acceptor (D-A) organic conjugated polymers (CPs) with the advantages of good biocompatibility, good photostability, and large extinction coefficient, have gradually become the widely studied nanoprobes for PA imaging-guided phototherapy [213–216]. For example, Guo *et al.* polymerized the alkyl-chain-grafted donor BDT (benzothiodiphene) and acceptor BBT (benzobisthiadiazole) to form D-A structured CPs (P1) [217]. P1 and DSPE-PEG2000-MAL combined to further form P1 NPs which were further decorated cyclo(Arg-Gly-Asp-D-Phe-Lys(mpa)) for selective targeting of tumor cells (Fig. 7c). The P1-RGD NPs have strong absorption in NIR-II region and can act as a PA imaging nanoprobe to clearly localize gliomas at a depth of nearly 3 mm through the scalp and skull (Fig. 7d). In addition, the PA images can reflect the accumulation and clearance of P1-RGD NPs in glioma in real time and guide photothermal treatment. And the PA imaging-guided PTT treatment also can avoid thermal damage to surrounding nerves and brain tissues, and maximize the photothermal effect on the tumor (Fig. 7e). By this D-A structure, the absorption wavelength of PA imaging nanoprobes can be extended to NIR-II region, providing a new strategy for the development of integrated probes for tumor diagnosis and therapy.

6. Summary and outlook

In summary, effective imaging nanoprobes have exhibited great potential in various medical imaging modalities, enabling precise imaging-guided tumor diagnosis and therapy. In addition, they are also powerful tools to achieve the delivery of anti-tumor drugs and tumor photodynamic therapy and phototherapy under the guidance of imaging. And imaging probes lay the foundation for the realization of precise clinical tumor therapy. Although the emergence of various nanoprobes with excellent properties will promote the advancement of medical imaging and precise tumor therapy, in the future, there is still room for further improvement in this area: (1) Utilizing surface/interface chemistry to further enhance the specific targeting ability of nanoprobes and improve the delivery efficiency of imaging nanoprobes *in vivo*. (2) Design biodegradable and highly biocompatible nanoprobes to reduce the residual amount of nanoprobes *in vivo* and decrease the toxicity. Nanomaterials may induce potential side effects at the cellular, tissue and organ system levels, with harmful consequences for patients treated with nanomaterials. For example, nanomaterials that remain in organisms for too long may cause side effects such cell death, oxidative stress and inflammation. (3) The non-invasive cross-scale imaging *in vivo* can provide more precise and comprehensive information on tumor development, classification, and staging. Thus, by designing and constructing multifunctional nanoprobes with multiple imaging functions, they will take an important part in multimodal imaging and play complementary roles in imaging depth, scope, and resolution. At present, imaging-guided surgical navigation and tumor phototherapy and chemotherapy are in the early stage of development, and with the development of precise imaging, the field will have better prospects in the future.

Declaration of competing interest

The authors declare that they have no known competing financial interests or personal relationships that could have appeared to influence the work reported in this paper.

Acknowledgments

This work was supported by the National Key R&D Program of China (No. 2020YFA0908800), the National Natural Science Foundation of China (Nos. 22174105 and 21974104), and Large-scale Instrument and Equipment Sharing Foundation of Wuhan University.

Supplementary materials

Supplementary material associated with this article can be found, in the online version, at doi:10.1016/j.cclet.2023.108460.

References

[1] D.Z. Li, H.D. Chen, F. Bi, Z.X. Wang, Chin. J. Anal. Chem. 44 (2016) 1609–1618.
[2] H. Peng, T. Wang, G. Li, J. Huang, Q. Yuan, Anal. Chem. 94 (2022) 1070–1075.
[3] F. Bray, M. Laversanne, E. Weiderpass, I. Soerjomataram, Cancer 127 (2021) 3029–3030.
[4] Y. Wang, W. Zhen, X. Jiang, J. Li, Small Sci. 2 (2022) 2100117.
[5] T. Hussain, Q.T. Nguyen, Adv. Drug Deliv. Rev. 66 (2014) 90–100.
[6] C. Li, G. Chen, Y. Zhang, F. Wu, Q. Wang, J. Am. Chem. Soc. 142 (2020) 14789–14804.
[7] M.R. Horsman, L.S. Mortensen, J.B. Petersen, M. Busk, J. Overgaard, Nat. Rev. Clin. Oncol. 9 (2012) 674–687.
[8] Z. Hu, C. Fang, B. Li, et al., Nat. Biomed. Eng. 4 (2020) 259–271.
[9] P. He, Y. Xiong, J. Ye, et al., J. Nanobiotechnol. 20 (2022) 250.
[10] J. Xu, W.W. Zhao, S. Song, C. Fan, H.Y. Chen, Chem. Soc. Rev. 43 (2014) 1601–1611.
[11] S. Song, Y. Qin, Y. He, et al., Chem. Soc. Rev. 39 (2010) 4234–4243.
[12] E.K. Lim, T. Kim, S. Paik, et al., Chem. Rev. 115 (2015) 327–394.
[13] D.E. Lee, H. Koo, I.C. Sun, et al., Chem. Soc. Rev. 41 (2012) 2656–2672.
[14] J. Wang, X. Wu, P. Shen, et al., Int. J. Nanomed. 15 (2020) 1903–1914.
[15] Y. Shi, J. Liu, Y. Zhang, et al., Chin. Chem. Lett. 32 (2021) 3189–3194.
[16] J. Key, J.F. Leary, Int. J. Nanomed. 9 (2014) 711–726.
[17] Y. Liu, P. Bhattarai, Z. Dai, X. Chen, Chem. Soc. Rev. 48 (2019) 2053–2108.
[18] J. He, H.F. VanBrocklin, B.L. Franc, Y. Seo, E.F. Jones, Curr. Nanosci. 4 (2008) 17–29.
[19] R.A. Sperling, W.J. Parak, Phil. Trans. R. Soc. A 368 (2010) 1333–1383.
[20] J. Schubert, M. Chanana, Curr. Med. Chem. 25 (2018) 4553–4586.
[21] M. Izci, C. Maksoudian, B.B. Manshian, S.J. Soenen, Chem. Rev. 121 (2021) 1746–1803.
[22] Z. Sheng, B. Guo, D. Hu, et al., Adv. Mater. 30 (2018) 1800766.
[23] P. Pei, Y. Chen, C. Sun, et al., Nat. Nanotechnol. 16 (2021) 1011–1018.
[24] A.L. Antaris, H. Chen, S. Diao, et al., Nat. Commun. 8 (2017) 15269.
[25] J.A. Carr, D. Franke, J.R. Caram, et al., Proc. Natl. Acad. Sci. U. S. A. 115 (2018) 4465–4470.
[26] H. Zhou, S. Li, X. Zeng, et al., Chin. Chem. Lett. 31 (2020) 1382–1386.
[27] J.T. Robinson, G. Hong, Y. Liang, et al., J. Am. Chem. Soc. 134 (2012) 10664–10669.
[28] X. Dang, L. Gu, J. Qi, et al., Proc. Natl. Acad. Sci. U. S. A 113 (2016) 5179–5184.
[29] Y. Fan, P. Wang, Y. Lu, et al., Nat. Nanotechnol. 13 (2018) 941–946.
[30] Y. Fan, F. Zhang, Adv. Opt. Mater. 7 (2019) 1801417.
[31] H. Yang, H. Huang, X. Ma, et al., Adv. Mater. 33 (2021) 2103953.
[32] Y. Zhan, S. Ling, H. Huang, et al., Angew. Chem. Int. Ed. 60 (2021) 2637–2642.
[33] C. Li, Q. Wang, Adv. Ther. 2 (2019) 1900053.
[34] M. Zhang, J. Yue, R. Cui, et al., Proc. Natl. Acad. Sci. U. S. A. 115 (2018) 6590–6595.
[35] X.L. Ge, B. Huang, Z.L. Zhang, et al., J. Mater. Chem. B 7 (2019) 5782–5788.
[36] L.L. Chen, L. Zhao, Z.G. Wang, S.L. Liu, D.W. Pang, Small 18 (2022) 2104567.
[37] W. Wang, Z. Ma, S. Zhu, et al., Adv. Mater. 30 (2018) 1800106.
[38] D. Huang, S. Lin, Q. Wang, et al., Adv. Funct. Mater. 29 (2019) 1806546.
[39] H. Huang, Z. Sun, H. Yang, et al., Nano Today 43 (2022) 101378.
[40] M.Y. Zhang, A.A. Liu, H. Fu, et al., Chem. Mater. 33 (2021) 9524–9533.
[41] Y. Zhang, H. Yang, X. An, et al., Small 16 (2020) 2001003.
[42] G.T. Yu, M.Y. Luo, H. Li, et al., ACS Nano 13 (2019) 12830–12839.
[43] C. Song, Y. Zhang, C. Li, et al., Adv. Funct. Mater. 26 (2016) 4192–4200.
[44] S. Ling, X. Yang, C. Li, et al., Angew. Chem. Int. Ed. Engl. 59 (2020) 7219–7223.
[45] X. Hao, C. Li, Y. Zhang, et al., Adv. Mater. 30 (2018) 1804437.
[46] F. Hu, C. Li, Y. Zhang, et al., Nano Res. 8 (2015) 1637–1647.
[47] Z.Y. Liu, A.A. Liu, H. Fu, et al., J. Am. Chem. Soc. 143 (2021) 12867–12877.
[48] Q. Ma, J. Wang, Z. Li, et al., Small 15 (2019) 1804969.
[49] D.J. Naczynski, M.C. Tan, M. Zevon, et al., Nat. Commun. 4 (2013) 2199.
[50] L. Li, L. Zhu, C. Ma, et al., Nat. Biomed. Eng. 1 (2017) 0071.
[51] I. Steinberg, D.M. Huland, O. Vermesh, et al., Photoacoustics 14 (2019) 77–98.
[52] L. Lin, P. Hu, J. Shi, et al., Nat. Commun. 9 (2018) 2352.
[53] P. Zhang, L. Li, L. Lin, J. Shi, L.V. Wang, Light Sci. Appl. 8 (2019) 36.
[54] P. Zhang, L. Li, L. Lin, et al., Biophotonics 11 (2018) 201700024.
[55] P.K. Upputuri, M. Pramanik, Wiley Interdiscip. Rev. Nanomed. Nanobiotechnol. 12 (2020) 1618.
[56] L.V. Wang, J. Yao, Nat. Methods 13 (2016) 627–638.
[57] P. Beard, Interface Focus 1 (2011) 602–631.
[58] F. Jansen, M. Lamla, D. Mauthe, et al., Rapid Commun. 41 (2020) 2000418.
[59] S. Wang, J. Lin, T. Wang, X. Chen, P. Huang, Theranostics 6 (2016) 2394–2413.
[60] J. Jung, Y. Jang, M. Kim, H. Kim, Photonics 8 (2021) 287.
[61] Y. Mantri, J.V. Jokerst, ACS Nano 14 (2020) 9408–9422.
[62] S.J. Yoon, A. Murthy, K.P. Johnaston, K.V. Sokolov, S.Y. Emelianov, Opt. Express 20 (2012) 29479–29487.
[63] B. Wang, Jimmy L. Su, J. Amirian, et al., Opt. Express 18 (2010) 4889–4897.
[64] D.J. Grootendorst, J. Jose, M.W. Wouters, et al., Lasers Surg. Med. 44 (2012) 541–549.
[65] A. Danielli, K. Maslov, C.P. Favazza, J. Xia, L.V. Wang, Appl. Phys. Lett. 106 (2015) 203701.
[66] A.J. Sinnamon, M.G. Neuwirth, Y. Song, et al., J. Surg. Oncol. 119 (2019) 1070–1076.
[67] Q. Fu, R. Zhu, J. Song, H. Yang, X. Chen, Adv. Mater. 31 (2019) 1805875.
[68] J.W. Kim, E.I. Galanzha, E.V. Shashkov, H.M. Moon, V.P. Zharov, Nat. Nanotechnol. 4 (2009) 688–694.
[69] W.J. Lee, E.Y. Park, D. Choi, et al., ACS Appl. Mater. Interfaces 12 (2020) 32270–32277.
[70] H. Moon, D. Kumar, H. Kim, et al., ACS Nano 9 (2015) 2711–2719.
[71] Y. Zhong, Y. Zou, L. Liu, et al., Acta Biomater. 115 (2020) 358–370.
[72] X. Zhen, K. Pu, X. Jiang, Small 17 (2021) 2004723.
[73] D. Ding, W. Guo, C. Guo, et al., Nanoscale 9 (2017) 2020–2029.
[74] Z. Sun, Y. Zhao, Z. Li, et al., Small 13 (2017) 1602896.
[75] Y. Liu, H. Liu, H. Yan, et al., Adv. Sci. 6 (2019) 1801615 Weinh.
[76] B. Guo, J. Chen, N. Chen, et al., Adv. Mater. 31 (2019) 1808355.
[77] W. Li, Z. Guo, Q. Tai, et al., Chin. Chem. Lett. 31 (2020) 2447–2451.
[78] J. Sun, R. Luo, Y. Xia, Chin. Chem. Lett. 31 (2020) 1946–1950.
[79] J. Chen, Z. Ye, F. Yang, Y. Yin, Small Sci. 1 (2021) 2000055.
[80] X. Yang, M. Yang, B. Pang, M. Vara, Y. Xia, Chem. Rev. 115 (2015) 10410–10488.
[81] D. Luo, X. Wang, C. Burda, J.P. Basilion, Cancers 13 (2021) 1825 Basel.
[82] Y. Pan, S. Neuss, A. Leifert, et al., Small 3 (2007) 1941–1949.
[83] A.M. Schrand, M.F. Rahman, S.M. Hussain, et al., Adv. Rev. 2 (2010) 544–568.
[84] X. Cheng, R. Sun, L. Yin, et al., Adv. Mater. 29 (2017) 1604894.
[85] Y.S. Chen, Y. Zhao, S.J. Yoon, S.S. Gambhir, S. Emelianov, Nat. Nanotechnol. 14 (2019) 465–472.
[86] J. Chen, C. Ning, Z. Zhou, et al., Prog. Mater. Sci. 99 (2019) 1–26.
[87] X. Chen, J. Yang, T. Wu, et al., Nanoscale 10 (2018) 15130–15163.
[88] G. Ku, M. Zhou, S. Song, et al., ACS Nano 6 (2012) 7489–7496.
[89] J. Li, J. Rao, K. Pu, Biomaterials 155 (2018) 217–235.
[90] X. Zhen, X. Feng, C. Xie, Y. Zheng, K. Pu, Biomaterials 127 (2017) 97–106.
[91] Y. Jiang, P.K. Upputuri, C. Xie, et al., Nano Lett. 17 (2017) 4964–4969.
[92] C. Yin, X. Zhen, H. Zhao, et al., ACS Appl. Mater. Interfaces 9 (2017) 12332–12339.
[93] Y. Jiang, P.K. Upputuri, C. Xie, et al., Adv. Mater. 31 (2019) 1808166.
[94] K. Pu, J. Mei, J.V. Jokerst, et al., Adv. Mater. 27 (2015) 5184–5190.
[95] F. Bruno, F. Arrigoni, S. Mariani, et al., Radiol. Med. 124 (2019) 243–252.
[96] Z. Zhou, Z.R. Lu, Wiley Interdiscip. Rev. Nanomed. Nanobiotechnol. 5 (2013) 1–18.
[97] V. Haribabu, K. Girigoswami, P. Sharmiladevi, A. Girigoswami, ACS Biomater. Sci. Eng. 6 (2020) 4377–4389.
[98] S.D. Serai, M.L. Ho, M. Artunduaga, S.S. Chan, G.B. Chavhan, Pediatr. Radiol. 51 (2021) 716–723.
[99] M. Nazarpoor, H. Fattahi, Nanomed. J. 6 (2019) 214–222.
[100] A. Avasthi, C. Caro, E. Pozo-Torres, M.P. Leal, M.L. Garcia-Martin, Top. Curr. Chem. 378 (2020) 40 Cham.
[101] F. Li, Z. Liang, J. Liu, et al., Nano Lett. 19 (2019) 4213–4220.
[102] J. Lu, J. Sun, F. Li, et al., J. Am. Chem. Soc. 140 (2018) 10071–10074.
[103] J. Wahsner, E.M. Gale, A. Rodriguez-Rodriguez, P. Caravan, Chem. Rev. 119 (2019) 957–1057.
[104] Q. Weng, X. Hu, J. Zheng, et al., ACS Nano 13 (2019) 6801–6812.
[105] S.H. Chen, L.Y. Huang, B. Huang, et al., ACS Appl. Mater. Interfaces 14 (2022) 11167–11176.
[106] Z. Ding, H. Sun, S. Ge, et al., Adv. Funct. Mater. 29 (2019) 1903860.
[107] L. Yang, C. Sun, H. Lin, et al., Chem. Mater. 31 (2019) 1381–1390.
[108] G. Jiang, D. Fan, J. Tian, Z. Xiang, Q. Fang, Adv. Healthc. Mater. 11 (2022) 2200841.
[109] X. Li, H. Zhou, Z. Niu, et al., ACS Appl. Mater. Interfaces 12 (2020) 24644–24654.
[110] C. Tullio, L. Salvioni, M. Bellini, et al., ACS Appl. Bio Mater. 4 (2021) 7800–7810.
[111] L. Yang, L. Wang, G. Huang, et al., Theranostics 11 (2021) 6966–6982.
[112] M. Ma, H. Zhu, J. Ling, et al., ACS Nano 14 (2020) 4036–4044.
[113] Y. Li, X. Zhao, X. Liu, et al., Adv. Mater. 32 (2020) 1906799.
[114] S. He, J. Song, J. Qu, Z. Cheng, Chem. Soc. Rev. 47 (2018) 4258–4278.
[115] H. Yuan, H. Liang, P. Hou, J. Li, Chem. Res. Chin. Univ. 37 (2021) 840.
[116] S.Y. Lee, S.I. Jeon, S. Jung, I.J. Chung, C.H. Ahn, Adv. Drug Deliv. Rev. 76 (2014) 60–78.
[117] M. Swierczewska, S. Lee, X. Chen, Mol. Imaging 10 (2011) 3–16.
[118] M.F. Kircher, A. de la Zerda, J.V. Jokerst, et al., Nat. Med. 18 (2012) 829–834.
[119] S. Hernot, L. van Manen, P. Debie, J.S.D. Mieog, A.L. Vahrmeijer, Lancet Oncol. 20 (2019) e354–e367.
[120] M.A. Stammes, S.L. Bugby, T. Porta, et al., Br. J. Surg. 105 (2018) e69–e83.
[121] C. Chi, Y. Du, J. Ye, et al., Theranostics 4 (2014) 1072–1084.
[122] F. Wang, L. Qu, F. Ren, et al., Proc. Natl. Acad. Sci. U. S. A. 119 (2022) e2123111119.
[123] M. Kamimura, Anal. Sci. 37 (2021) 691–697.
[124] Z. Ma, M. Zhang, J. Yue, et al., Adv. Funct. Mater. 28 (2018) 1803417.
[125] N. Zhang, C. Lu, M. Chen, et al., J. Nanobiotechnol. 19 (2021) 132.
[126] P. Wang, Y. Fan, L. Lu, et al., Nat. Commun. 9 (2018) 2898.
[127] R. Tian, H. Ma, S. Zhu, et al., Adv. Mater. 32 (2020) 1907365.
[128] C. Li, L. Cao, Y. Zhang, et al., Small 11 (2015) 4517–4525.
[129] R. Yan, Y. Hu, F. Liu, et al., J. Am. Chem. Soc. 141 (2019) 10331–10341.
[130] C. Wang, W. Fan, Z. Zhang, et al., Adv. Mater. 31 (2019) 1904329.
[131] Z. Fan, B. Jiang, Q. Zhu, et al., ACS Appl. Mater. Interfaces 12 (2020) 14884–14904.
[132] Y. Li, G. Liu, J. Ma, et al., J. Control. Release 258 (2017) 95–107.
[133] B. Shi, N. Ren, L. Gu, et al., Angew. Chem. Int. Ed. 58 (2019) 16826–16830.
[134] G. Wang, Y. Ma, Z. Wei, M. Qi, Chem. Eng. J. 289 (2016) 150–160.
[135] J. Huang, W. Huang, Y. Chen, et al., RSC Adv. 8 (2018) 41956–41965.
[136] Y. Guo, X.Y. Wang, Y.L. Chen, et al., Acta Biomater. 80 (2018) 308–326.
[137] G. Yu, Z. Yang, X. Fu, et al., Nat. Commun. 9 (2018) 766.
[138] Y. Wang, H. Wang, D. Liu, et al., Biomaterials 34 (2013) 7715–7724.

[139] P. Nicolino, S. Mario, S. Mario, Int. J. Nanomed. 9 (2014) 467–483.
[140] Z. Zhou, Z.R. Lu, Adv. Drug Deliv. Rev. 113 (2017) 24–48.
[141] L. Bejarano, M.J.C. Jordão1, J.A. Joyce, Cancer Discov. 11 (2021) 933–959.
[142] Q. Zhou, L. Zhang, T. Yang, H. Wu, Int. J. Nanomed. 13 (2018) 2921–2942.
[143] M. Vallet-Regi, M. Colilla, I. Izquierdo-Barba, M. Manzano, Molecules 23 (2017) 47.
[144] J. Liu, Y. Huang, A. Kumar, et al., Biotechnol. Adv. 32 (2014) 693–710.
[145] Y. Lu, J. Feng, Z. Liang, et al., Nanoscale Horiz. 7 (2022) 403–413.
[146] M. Wu, Y. Xue, N. Li, et al., Angew. Chem. Int. Ed. 58 (2019) 6880–6885.
[147] W. Zhang, Z. Huang, X. Pu, et al., Chin. Chem. Lett. 31 (2020) 285–291.
[148] H. Chen, Z. Zhen, W. Tang, et al., Theranostics 3 (2013) 650–657.
[149] L. Zhang, C.X. Li, S.S. Wan, X.Z. Zhang, Adv. Healthc. Mater. 11 (2022) 2101971.
[150] X. Meng, X. Zhang, M. Liu, et al., Appl. Mater. Today 21 (2020) 100864.
[151] X. Wang, X. Zhong, Z. Liu, L. Cheng, Nano Today 35 (2020) 100946.
[152] L.S. Lin, T. Huang, J. Song, et al., J. Am. Chem. Soc. 141 (2019) 9937–9945.
[153] Y. Zhu, Y. Wang, G.R. Williams, et al., Adv. Sci. 7 (2020) 2000272.
[154] P. Manivasagan, A. Joe, H.W. Han, et al., Mater. Today Bio 13 (2022) 100197.
[155] Z. Tang, Y. Liu, M. He, W. Bu, Angew. Chem. Int. Ed. 58 (2019) 946–956.
[156] C. Jia, Y. Guo, F.G. Wu, Small 18 (2022) 2103868.
[157] P. Liu, Y. Peng, J. Ding, W. Zhou, Asian J. Pharm. Sci. 17 (2022) 177–192.
[158] Q. Chen, X. Ma, L. Xie, et al., Nanoscale 13 (2021) 4855–4870.
[159] J. Xin, C. Deng, O. Aras, et al., J. Nanobiotechnol. 19 (2021) 192.
[160] C. Zhang, W. Bu, D. Ni, et al., Angew. Chem. Int. Ed. 55 (2016) 2101–2106.
[161] Y. Liu, X. Ji, W.W.L. Tong, et al., Angew. Chem. Int. Ed. 57 (2018) 1510–1513.
[162] J.X. Fan, M.Y. Peng, H. Wang, et al., Adv. Mater. 31 (2019) 1808278.
[163] L.H. Fu, C. Qi, Y.R. Hu, J. Lin, P. Huang, Adv. Mater. 31 (2019) 1808325.
[164] C. Xie, D. Cen, Z. Ren, et al., Adv. Sci. 7 (2020) 1903512.
[165] M. Chang, Z. Hou, D. Jin, et al., Adv. Mater. 32 (2020) 2004647.
[166] P. Zhao, Z. Tang, X. Chen, et al., Mater. Horiz. 6 (2019) 369–374.
[167] J. Li, K. Yi, Y. Lei, et al., Chem. Commun. 56 (2020) 6285–6288.
[168] S. Koo, O.K. Park, J. Kim, et al., ACS Nano 16 (2022) 2535–2545.
[169] C. Dong, W. Feng, W. Xu, et al., Adv. Sci. 7 (2020) 2001549.
[170] R. Hu, Y. Fang, M. Huo, et al., Biomaterials 206 (2019) 101–114.
[171] Y. Liu, J. Wu, Y. Jin, et al., Adv. Funct. Mater. 29 (2019) 1904678.
[172] J. Zuo, X. Gao, J. Xiao, Y. Cheng, Chin. Chem. Lett. 34 (2023) 107827.
[173] X. Yu, H. Ma, G. Xu, Z. Liu, Chin. Chem. Lett. 33 (2022) 4169–4174.
[174] M.R. Younis, G. He, J. Qu, et al., Adv. Sci. 8 (2021) 2102587.
[175] N. Jiang, Z. Zhou, W. Xiong, et al., Chin. Chem. Lett. 32 (2021) 3948–3953.
[176] J. Liu, J. Shi, W. Nie, et al., Adv. Healthc. Mater. 10 (2021) 2001207.
[177] R. Wu, H. Wang, L. Hai, et al., Chin. Chem. Lett. 31 (2020) 189–192.
[178] D. Wang, M.M.S. Lee, W. Xu, et al., Theranostics 8 (2018) 4925–4956.
[179] H. Lin, Z. Lin, K. Zheng, et al., Adv. Opt. Mater. 9 (2021) 2002177.
[180] B. del Rosal, B. Jia, D. Jaque, Adv. Funct. Mater. 28 (2018) 1803733.
[181] K. Siwawannapong, R. Zhang, H. Lei, et al., Theranostics 10 (2020) 62–73.
[182] P. Sarbadhikary, B.P. George, H. Abrahamse, Theranostics 11 (2021) 9054–9088.
[183] R. Jia, H. Xu, C. Wang, et al., J. Nanobiotechnol. 19 (2021) 419.
[184] T. Li, L. Liu, P. Xu, et al., Adv. Ther. 4 (2020) 2000240.
[185] T. Li, C. Li, Z. Ruan, et al., ACS Nano 13 (2019) 3691–3702.
[186] Z. Yu, C. Eich, L.J. Cruz, Front. Chem. 8 (2020) 496.
[187] N. Mauro, M.A. Utzeri, A. Sciortino, et al., ACS Appl. Mater. Interfaces 14 (2022) 2551–2563.
[188] P. Huang, J. Lin, X. Wang, et al., Adv. Mater. 24 (2012) 5104–5110.
[189] M. Jiao, Y. Wang, W. Wang, et al., Chem. Eng. J. 440 (2022) 135965.
[190] N. Yang, W. Xiao, X. Song, W. Wang, X. Dong, Nano Micro Lett. 12 (2020) 15.
[191] G. Yang, L. Xu, J. Xu, et al., Nano Lett. 18 (2018) 2475–2484.
[192] L. Huang, S. Zhao, J. Wu, et al., Coord. Chem. Rev. 438 (2021) 213888.
[193] Q. Jia, J. Ge, W. Liu, et al., Adv. Mater. 30 (2018) 1706090.
[194] J. Dai, X. Wu, S. Ding, et al., J. Med. Chem. 63 (2020) 1996–2012.
[195] D. Mao, F. Hu, Z. Yi, et al., Sci. Adv. 6 (2020) eabb2712.
[196] A. Reisch, A.S. Klymchenko, Small 12 (2016) 1968–1992.
[197] P. Huang, J. Lin, S. Wang, et al., Biomaterials 34 (2013) 4643–4654.
[198] S. Ren, X. Cheng, M. Chen, et al., ACS Appl. Mater. Interfaces 9 (2017) 31509–31518.
[199] S. Yang, C. Chen, Y. Qiu, C. Xu, J. Yao, Biomaterials 268 (2021) 120562.
[200] B. Huang, J. Hu, H. Li, et al., ACS Appl. Bio Mater. 3 (2020) 1636–1645.
[201] X. Li, M. Jiang, S. Zeng, H. Liu, Theranostics 9 (2019) 3866–3878.
[202] L. Chen, W. Zuo, Z. Xiao, et al., J. Colloid Interface Sci. 600 (2021) 243–255.
[203] L. Xie, G. Wang, H. Zhou, et al., Biomaterials 103 (2016) 219–228.
[204] F. Wang, C. Song, W. Guo, et al., New J. Chem. 41 (2017) 14179–14187.
[205] R. Kawasaki, K. Kondo, R. Miura, et al., Int. J. Mol. Sci. 23 (2022) 4686.
[206] T. Yang, Y. Tang, L. Liu, et al., ACS Nano 11 (2017) 1848–1857.
[207] E.V. Shashkov, M. Everts, E.I. Galanzha, V.P. Zharov, Nano Lett. 8 (2008) 3953–3958.
[208] Y. Jiang, J. Li, Z. Zeng, et al., Angew. Chem. Int. Ed. Engl. 58 (2019) 8161–8165.
[209] H. Li, Y. Li, A. Aljarb, Y. Shi, L.J. Li, Chem. Rev. 118 (2018) 6134–6150.
[210] X. Jiang, Y. Han, H. Zhang, et al., ACS Appl. Mater. Interfaces 10 (2018) 43396–43404.
[211] Z.H. Miao, L.X. Lv, K. Li, et al., Small 14 (2018) 1703789.
[212] T. Guo, Q. Tang, Y. Guo, et al., Appl. Mater. Interfaces 13 (2021) 306–311.
[213] B. Guo, G. Feng, P.N. Manghnani, et al., Small 12 (2016) 6243–6254.
[214] X. Fu, H. Bai, F. Lyu, L. Liu, S. Wang, Chem. Res. Chin. Univ. 36 (2020) 237–242.
[215] Y.L. Zhang, J.T. Ren, H.Y. Gao, et al., Chin. J. Polym. Sci. 38 (2020) 814–818.
[216] Z. Cheng, T. Zhang, W. Wang, et al., Chin. Chem. Lett. 32 (2021) 1580–1585.
[217] B. Guo, Z. Sheng, D. Hu, et al., Adv. Mater. 30 (2018) 1802591.